Chapter 4 Evidence for Spin Canting in $BaFe_{12}FO_{19}$ at T > 1.5 K

4.1 Introduction

In chapter 3, using X-ray magnetic circular dichroism (XMCD) studies we showed that in the magnetic ground state of $BaFe_{12}O_{19}$ (BFO) the $3dFe^{3+}$ spins are canted away from the c-axis. This implies that the magnetic structure of BFO deviates from the simple Ising like picture in the Gorter Model [39]. We also presented evidence for the precession of the Fe^{3+} spins around the c-direction leading to a conical magnetic structure as evidenced by the presence of magnetic satellite peaks in the single-crystal neutron diffraction pattern recorded along the *00l* reciprocal lattice row. These satellite peaks are forbidden as per the nuclear space group $P6_3/mmc$ and also the magnetic space group for the collinear Gorter Model $P6_3/mm'c'$ [131,136]. The presence of the satellite peaks also confirms that the Fe^{3+} spins are canted. In this chapter, we show that this canted structure survives even at high temperatures as revealed by large magnetic anisotropy ($A = \frac{M_{//c}}{M_{\perp c}}$) at all temperature below the Curie transition using direct current (dc) magnetization $M_{//c}(T)$ and $M_{\perp c}(T)$ measurements parallel (//c) and perpendicular ($\perp$c) to the c-axis, respectively. It is shown that the magnetic anisotropy ($A = \frac{M_{//c}}{M_{\perp c}}$) increases gradually below the Curie temperature (T_c), and shows a significant peak around T ~ 45 K, indicative of a finite spin component in the ab-plane which leads to a magnetic transition around 45 K. The spin canting at T > 1.2 K is further confirmed by the study of X-ray absorption spectra (XAS) and XMCD signals, measured on single-crystals of BFO in normal incidence (NI) and grazing incidence (GI) geometries, as a function of temperature upto 30 K. We have observed an inversion in the shape of the XMCD profile around 13.5 K whereby the valleys and peaks around the Fe-L_3 edge at T < 13.5 K become peaks and valleys,

respectively, at the same energies for T ≥ 13.5 K. To get an insight into the likely factors responsible for this profile shape inversion, we also investigated the state of hybridization of the 3dFe^{3+} orbitals with the 2p O^{2-} orbitals using XAS spectra recorded at the oxygen (O) K-edge. These studies reveal that the exchange energies are changing between 5.5 K and 13.5 K, which, we believe, may be responsible for the inversion of the XMCD profile shapes between the same temperatures. It is suggested that theoretical calculations are required to capture the effect of exchange energies on the XMCD profile shapes.

4.2 Experimental

The details of growth and characterization of BFO single crystals are already presented in chapter 2. The dc magnetization $M_{//c}$(T) and $M_{\perp c}$(T) measurements on zero-field cooled single crystals of BFO during the warming cycle was carried out under a magnetic field of 500 Oe applied parallel and perpendicular to the c-axis, respectively, in the temperature range 2 to 950 K in two steps, from 2 to 300 K and 300 K to 950 K, using the low and high-temperature measurement set-ups in a physical property measurement system (PPMS, DynaCool, Quantum Design, USA).

The temperature-dependent XAS and XMCD data at the Fe $L_{2,3}$-edges were obtained in the temperature range 1.2 K to 30 K for the normal incidence (NI) and grazing incidence (GI) geometries on BFO single crystals at the beam-line P04 of PETRA-III, Hamburg, Germany [208]. In the NI and GI geometries, the angle (θ) between the direction of propagation vector (**k**) of the circularly polarized soft X-ray beam and the normal to the (00*l*) plane of the hexagonal unit-cell was 0^0 and 15^0, respectively. Temperature-dependent XAS and XMCD signals were also measured with a magnetic field of 0.5 T applied along the **k**-vector of circularly polarised beam in the GI geometry. Further, XAS spectra were recorded in the 1.2 K to 30K range for the O-K edge also in the NI geometry.

4.3 Results and Discussion

4.3.1 DC Magnetization Studies

The first signature of the deviation from the Gorter model of collinear Ising spins of BFO at higher temperatures is revealed through the magnetic anisotropy of the dc magnetization M(T). The variation of $M_{\perp c}(T)$ and $M_{//c}(T)$, measured during the warming cycle on a zero-field cooled (ZFC) crystal, with a magnetic field of 500 Oe applied perpendicular ($\perp$) and parallel (//) to the c-axis of the unit cell, respectively, is shown in Fig. 4.1(a). These plots were obtained by merging the results of measurements in the 300 K to 950 K and 2 K to 300 K temperature range using high and low-temperature attachments in the PPMS system. To locate the LRO ferrimagnetic transition temperature, i.e., the Curie temperature (T_c), we use the first derivative of $M_{\perp c}(T)$ and $M_{//c}(T)$ curves with respect to temperature (T). This derivative plot is depicted in Fig. 4.1(b) on a zoomed scale. The 1st derivative of $M_{//c}(T)$ shows a valley at T_c ~714 K while 1st derivative of $M_{\perp c}(T)$ shows a similar valley at T_c ~ 707 K. There is a small difference of 7 K between the T_c obtained from the derivative plots of magnetization $M_{\perp c}(T)$ and $M_{//c}(T)$ curves which, we believe, is mainly due to the slight misorientation of the c-axis with respect to the magnetic field (H) direction. Since the platelet morphology of the crystal (as discussed in chapter 2) was such that aligning the c-axis parallel to the magnetic field was very accurate, the valley in the derivative of $M_{//c}(T)$ has been taken as the correct Curie temperature i.e. T_c ~ 714 K. This T_c is in good agreement with previous single-crystal measurements on BFO [220].

Above T_c in the paramagnetic region, the dc magnetic susceptibility is known to follow the Curie-Weiss law [38]:

$$\chi = \frac{C}{T - \Theta_{cw}}, \qquad \text{.....(4.1)}$$

where C is the Curie constant and Θ_{cw} is the Curie-Weiss temperature.

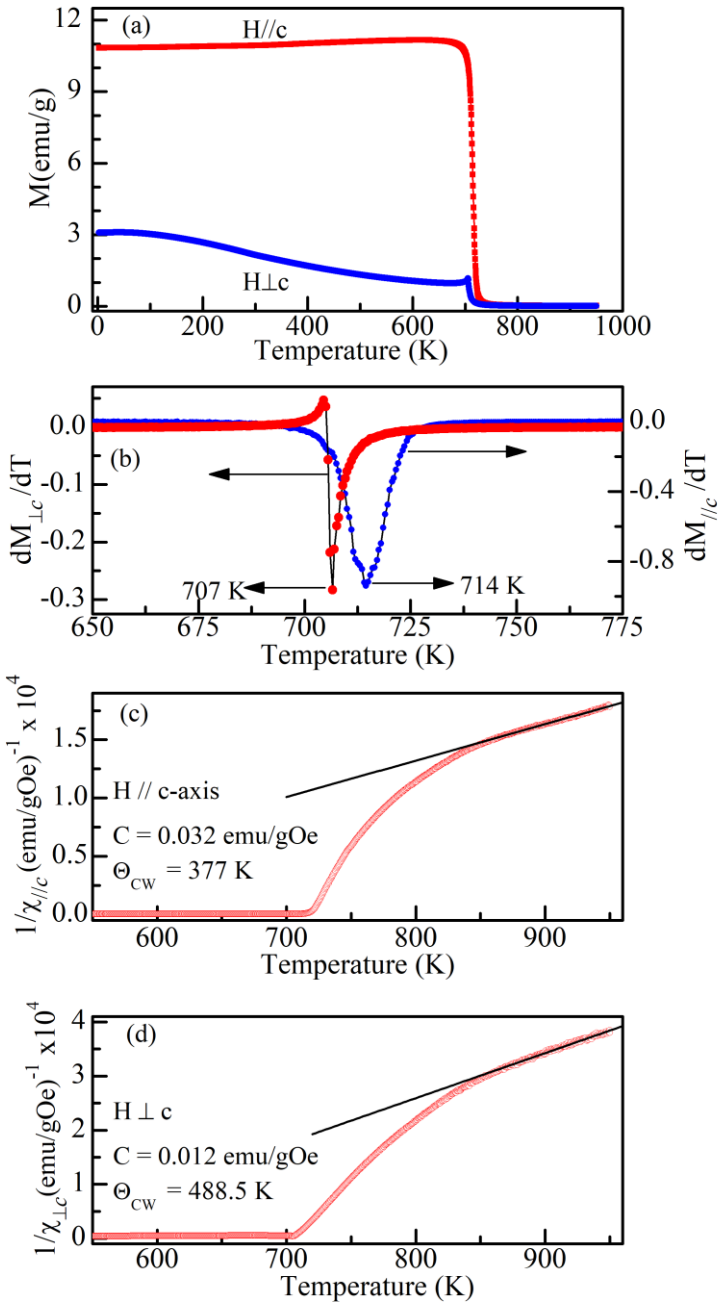

Figure 4.1: (a) Variation of the dc magnetization $M_{\perp c}$ and $M_{//c}$ measured with a field of 500 Oe applied parallel (//) and perpendicular ($\perp$) to the c-axis of the crystal. (b) The first derivative plot of $M_{\perp c}$ and $M_{//c}$ with respect to the temperature. (c) Curie-Weiss fit for $\chi_{//c}(T)$ and (d) $\chi_{\perp c}(T)$.

The magnitude of Θ_{cw} represents the strength of magnetic correlations. Its positive and negative signs signify the dominant interactions of the ferromagnetic and antiferromagnetic types, respectively. It is evident from Equation (4.1) that $1/\chi_{dc}$ versus T plot should be a straight-line curve. The Curie-Weiss fits to the inverse of $\chi_{//c}$ and $\chi_{\perp c}$ in the high-temperature region using the data along and perpendicular to c-axis are depicted in Figs. 4.1(c) and (d), respectively, for T > 850 K. The fitting parameters obtained after the least-squares fit are: C ~ 0.032 emu/g Oe, Θ_{CW} ~ 377 K for H//c and C ~ 0.012 emu/g Oe, Θ_{CW} ~ 488.5 K for H⊥c. The positive value of Θ_{CW} suggests dominant ferromagnetic type magnetic correlations in this system. However, the departure from Curie-Weiss behaviour above T_c ~ 714 K to T = 850 K range is notable and points towards the possible role of more than one magnetic sublattices due to the ferrimagnetic alignment of spins in BFO.

The variation of $M_{\perp c}$(T) and $M_{//c}$(T) below 300K, depicted in Fig. 4.2 on a magnified scale, reveals that $M_{\perp c}$(T) increases steadily with decreasing temperature upto ~ 45 K and then shows a peak at T ~ 45 K for the measuring field of 500 Oe (see inset of Fig. 4.2). This peak temperature increases on decreasing the field. In the earlier reports [137], this peak is not so well resolved as in Fig. 4.2 and no field dependence of the peak temperature was reported. Unlike the behaviour of $M_{\perp c}$(T), the magnetization parallel to the c-axis $M_{//c}$(T) decreases more or less continuously with decreasing temperature with a slight change of slope around 100 K. As shown in chapter 7, a very broad peak around 200 K due to another magnetic transition becomes discernible at higher measuring fields (e.g. 1000 Oe). The behaviour of $M_{\perp c}$(T) and $M_{//c}$(T) curves indicates that the spins may not be fully aligned along the c-axis at low temperatures. The variation of the anisotropy parameter A = $(\frac{M_{\perp c}}{M_{//c}})$ [152] with temperature, depicted in Fig.

4.3, shows that it increases with decreasing temperature below 600 K and peaks at T ~ 45 K confirming the existence of a transition in the ab-plane [152].

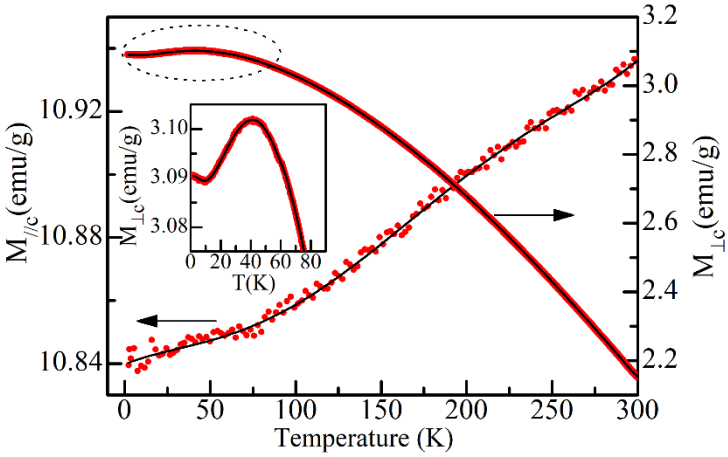

Figure 4.2: Magnified view of the temperature dependence of $M_{\perp c}$ and $M_{//c}$ in the 2 K to 300 K range, measured with a dc field of 500 Oe, during the warming cycle on a ZFC crystal. The inset shows the occurrence of a magnetic transition at low temperatures on a magnified scale in a smaller temperature range.

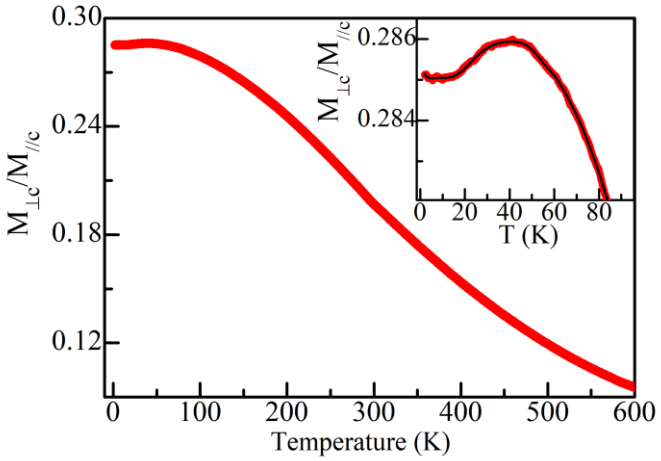

Figure 4.3: Variation of the magnetic anisotropy parameter A = $(\frac{M_{\perp c}}{M_{//c}})$ with temperature. Inset gives the magnified view in the vicinity of the transition temperature.

The values of magnetization measured with field-applied parallel and perpendicular to the c-axis reveal that ~ 28% of the spin component of $M_{//c}(T)$ lies in the ab-plane at T ~ 45 K. All these results suggest that the spins may not be fully aligned along the c-axis of BFO at low temperatures but may have a significant component transverse to the c-axis in the basal plane (00*l* plane) due to the canting of the spins away from the c-axis leading to a magnetic transition around 45 K. As shown in the next chapter, this transition has a spin-glass character.

4.3.2 XAS and XMCD Studies at the Fe $L_{2,3}$-edges from 1.2 to 30 K

In chapter 3, we presented evidence for non-collinear magnetic structure of BFO in its ground state (T < 2 K) using XMCD studies. In order to confirm the canting of the 3dFe^{3+} spins away from the c-axis above 1.2 K, we investigated the angle-dependent XMCD signals using XAS spectra recorded on a single-crystal of BFO upto 30 K. As in chapter 3 incident-flux (I_0)-normalized XAS spectra were measured in the NI and GI geometries for the right circularly polarized (RCP) and left circularly polarized (LCP) incident X-ray beams. Using the same protocols as discussed in section 3.5.1 of chapter 3, the linear background was subtracted from the incident-flux-normalized XAS spectra measured using RCP and LCP beams. After subtraction of the linear background, post edges of XAS spectra were normalised to 1. The post edge normalised XAS spectra at the $L_{2,3}$-edges of Fe measured using RCP and LCP X-ray beams are labelled as σ_+ and σ_-. The σ_+ and σ_- spectra of Fe at the $L_{2,3}$-edges measured in the NI geometry without magnetic field at 30 K, 13.5 K, 5.5 K and 1.2 K are shown in Figs. 4.4(a), (b), (c) and (d), respectively, where the results of 1.2 K are reproduced from the previous chapter for the sake of completeness. The XMCD signal $\Delta\sigma$ (= $\sigma_+ - \sigma_-$) of Fe at the $L_{2,3}$-edges at each temperature is shown in the same figures. Table 4.1 lists the energy of the peaks and valleys observed in the XMCD profiles at various temperatures. As discussed in chapter 3, Fe in BFO is

located in three different types of oxygen environments: trigonal bipyramid (TBP), tetrahedral (TH) and octahedral (OH). Therefore, one would expect signatures of these environments in the XMCD signals also. Based on our earlier discussion in section 3.5.1 of chapter 3, we assigned the prominent peak and valley in the XMCD signal at 1.2 K being due to Fe in the TH and OH environments (see Fig. 4.4(d)). On raising the temperature to 5.5 K, peak and valley due to Fe at the TH and OH environments become more prominent. However, on increasing the temperature further to 13.5 K, the XMCD profile shape gets is inverted i.e., the peak and valley due to Fe in TH and OH environments at 5.5 K turn into valley and peak at 13.5 K. On further raising the temperature at 30K, shape of the XMCD profile remains similar to that at 13.5 K except for the more prominent XMCD signal. Inversion of the XMCD signal at 13.5 K is probably related to the change in crystal field splitting energy and/or electronic exchange-correlation energy between 5.5 K and 13.5 K, which we have explored through temperature-dependent study of XAS spectra at the O K-edge measured in the same geometry (i.e., NI geometry) in a later section of this chapter.

In order to extract information about the basal plane spin component of the magnetic spins, we analysed the temperature-dependent XAS spectra of Fe at the $L_{2,3}$-edges recorded in the GI geometry with H = 0 T. Following the same protocols of linear background subtraction, as discussed in chapter 3, the post edge σ_+ and σ_- spectra of Fe were normalised to 1. The σ_+ and σ_- spectra of Fe thus obtained along with the XMCD signal in the GI geometry under zero-field bias (i.e., H = 0 T) are shown in Figs. 4.5 (a), (b), (c) and (d) for 30 K, 13.5 K, 5.5 K and 1.2 K, respectively. The energy of the peaks and valleys observed in XMCD profile at various temperatures are listed in Table 4.2. We find that the peak in the XMCD profile at ~ 709.5 eV at 1.2 K and 5.5 K changed to a

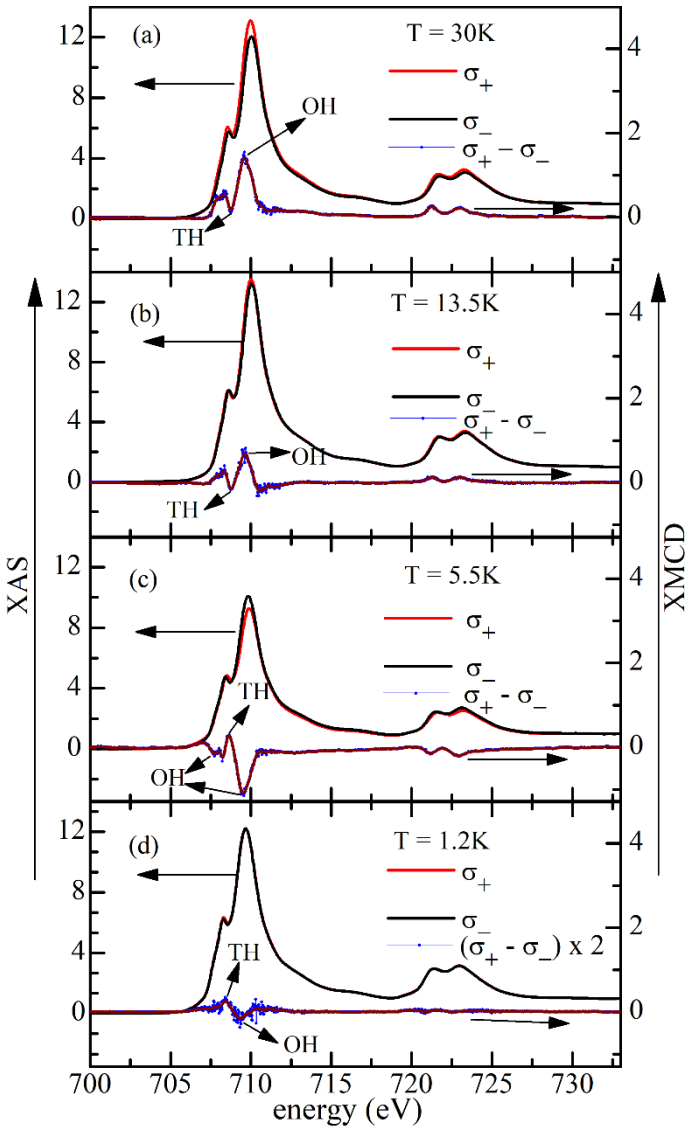

Figure 4.4: XAS spectra and XMCD signals at the Fe $L_{2,3}$-edges measured in the NI geometry without dc magnetic field bias measured at (a) 30 K, (b) 13.5 K, (c) 5.5 K and (d) 1.2 K. TH and OH in (a)-(d) stand for the tetrahedral and octahedral environments of Fe.

Table 4.1: Energy of the valleys and peaks in the XMCD profile of Fe at the L_3-edge measured in NI geometry with H = 0 T.

T (K)	Valley-1	Valley/Peak-2	Valley/Peak-3
1.2 K	--	~ 708.4 eV	~ 709.34 eV
5.5 K	~ 707.6 eV	~ 708.5 eV	~ 709.5 eV
13.5 K	--	~ 708.4 eV	~ 709.6 eV
30 K	--	~ 708.4 eV	~ 709.6 eV

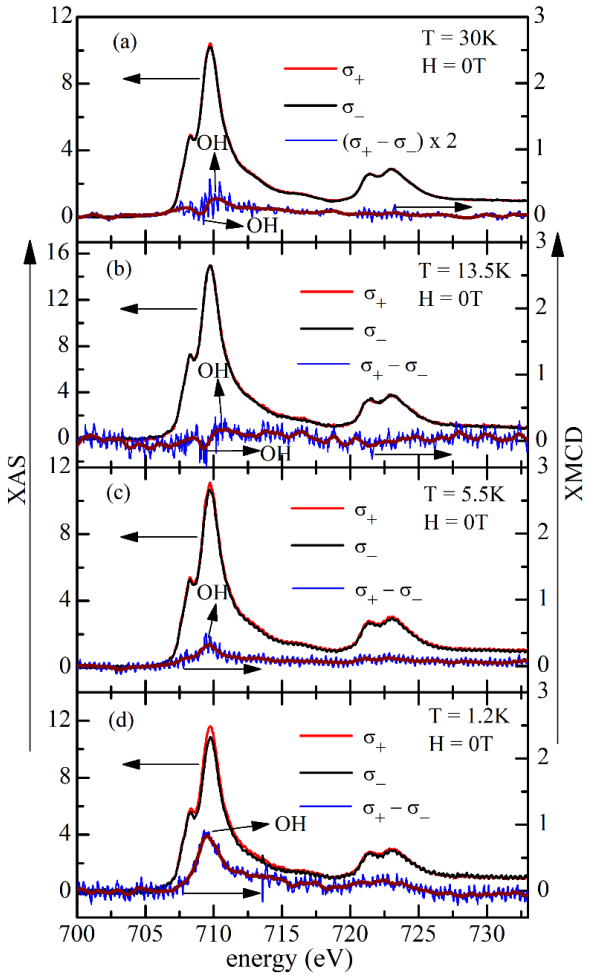

Figure 4.5: XAS spectra and XMCD signals of Fe at the $L_{2,3}$-edges measured in the GI geometry without dc magnetic field bias (H = 0 T) at (a) 30 K, (b) 13.5 K, (c) 5.5 K and (d) 1.2 K. OH in (a)-(d) stands for octahedral environments of Fe.

Table 4.2: Energy of valleys and peaks in the XMCD profile of Fe at the L_3-edge measured in GI geometry with H = 0 T.

T (K)	Peak-1	Peak-2	Valley-1
1.2 K	--	~ 709.5 eV	--
5.5 K	~ 708.0 eV	~ 709.6 eV	--
13.5 K	~ 708.47 eV	~ 710.25 eV	~ 709.25 eV
30 K	~ 707.7 eV	~ 710.2 eV	~ 709.15 eV

valley on increasing the temperature to T ≥ 13.5 K. Based on our earlier discussion, we argue that the peaks at ~ 709.5 eV in XMCD signal is due to Fe at OH environment. Further, the observed peak at ~ 710.25 eV marked in Figs. 4.5 (a) and (b) is also attributable to the Fe in the OH environments, as per Table 3.2 of chapter 3.

We also analysed the XAS spectra and XMCD signals in the GI geometry recorded under a dc bias field of H = 0.5 T applied parallel to the beam direction (see Fig. 4.6). The σ_+ and σ_- spectra of Fe along with XMCD signals measured in the GI geometry

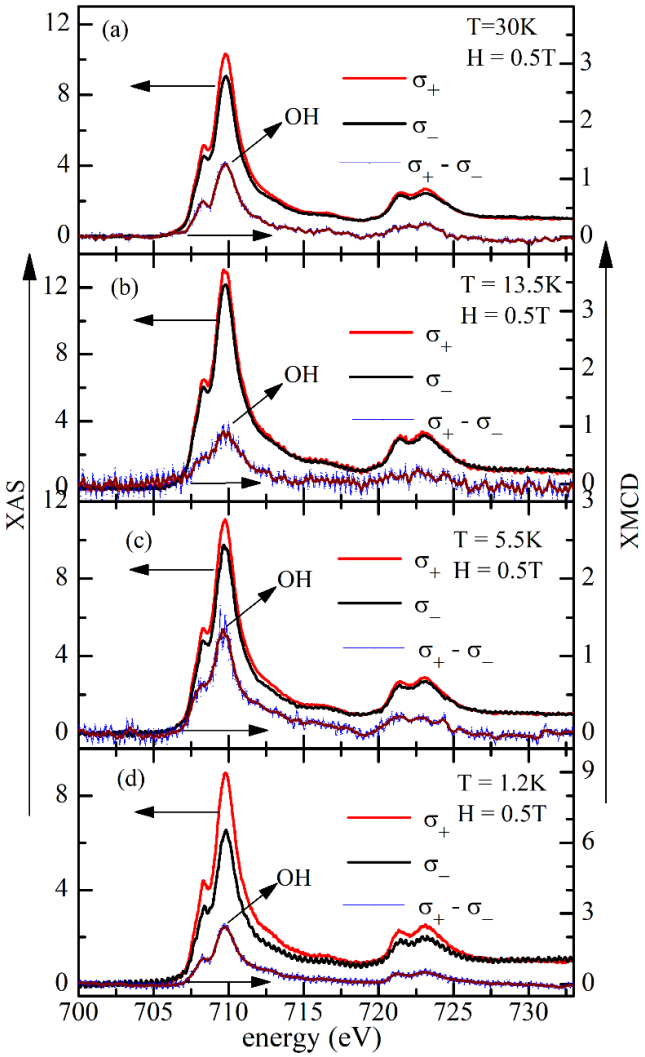

Figure 4.6: XAS spectra and XMCD signals of Fe at the $L_{2,3}$-edges measured in the GI geometry with a biasing magnetic field of H = 0.5 T at (a) 30 K, (b) 13.5 K, (c) 5.5 K and (d) 1.2 K. OH in (a)-(d) stand for octahedral environments of Fe.

at H = 0.5 T are shown in Figs. 4.6 (a), (b), (c) and (d) for 30 K, 13.5 K, 5.5 K and 1.2 K, respectively. The energy of the peaks and valleys observed in XMCD profile measured in GI geometry with field 0.5 T at various temperatures are listed in Table 4.3.

The presence of the significant XMCD signals in the GI geometry and its enhancement under dc bias field confirms that the Fe^{3+} spins are indeed canted away from the c-axis of BFO even above 1.2 K. It is also evident from Fig. 4.6 that XMCD signal in the GI geometry under H = 0.5 T shows a prominent peak at ~ 709.7 eV at all the four temperatures from 1.2 K to 30 K. In marked contrast, the XMCD signals in the GI geometry without magnetic field bias shown in Fig. 4.5 reveal that this peak at 1.2 K and 5.5 K changes over to a valley at the same energy for T ≥ 13.5 K. The energies of the XMCD profiles suggests that the major contribution to the XMCD signal with or without dc field bias for the GI geometry is still coming from Fe at the OH environment.

Table 4.3: Energy of valleys and peaks in the XMCD profile of Fe at the L_3-edge measured in GI geometry with H = 0.5 T.

T (K)	Peak-1	Peak-2
1.2 K	~ 708.2 eV	~ 709.7 eV
5.5 K	~ 708.2 eV	~ 709.6 eV
13.5 K	~ 708.14 eV	~ 709.7 eV
30 K	~ 708.2 eV	~ 709.7 eV

4.3.3 Variation of the Magnetic Moment obtained from XMCD and dc Magnetization Measurements with Temperature

Since the strength of the XMCD signal is directly related to the magnitude of the spin moments, we can estimate the magnitude of the spin magnetic moment using the following spin sum rule equation [211,217–219,221], as already discussed in the previous chapter:

$$m_{spin} + 7m_T^{\theta} = -\frac{(6P-4Q)\, n_h}{R}, \qquad \text{.....(4.2)}$$

where $P = \int_{L3}(\sigma_+ - \sigma_-)d\omega$, $Q = \int_{L3+L2}(\sigma_+ + \sigma_-)d\omega]$, $R = \int_{L3+L2}(\sigma_+ + \sigma_-)d\omega$, m_{spin} is the total spin magnetic moment in units of μ_B/formula unit, n_h is the number of Fe-3d holes, and $m_T^{\theta} = <T_\theta>\mu_B/\hbar$ with $<T_\theta>$ being the expectation value of magnetic dipole operator whose contribution is negligible for 3dFe^{3+} spins [202]. L_3 and L_2 represent the integration range over energies of the two absorption edges.

To estimate the spin magnetic moment (m_{spin}) using Equation (4.2), we need to first calculate the P, Q and R values using the XMCD signals and the XAS spectra recorded at each temperature. We have estimate the P, Q and R values by following the steps discussed in ref. [211] and already explained in chapter 3. First, we integrate the XMCD signal over the $L_{2,3}$ energy range and estimate the P and Q values. To integrate the sum of XAS spectra, we calculate the sum of XAS as sum XAS = $(\sigma_+ + \sigma_-)/2$, then we remove the edge jump using a two-step-like function and finally we integrate the sum XAS spectra over the $L_{2,3}$ energy range. Using the integrated sum XAS spectra we have estimated the value of R. The variation of the XAS (σ_+ and σ_-), XMCD (= $\sigma_+ - \sigma_-$), sum XAS and their integration for NI geometry with H = 0 T at 30 K, 13.5 K, 5.5 K and 1.2 K are shown in appendix A as Figs. A4.1(a)-(c), A4.1(d)-(f), A4.2(a)-(c) and A4.2(d)-(f), respectively. Similarly, the XAS, XMCD, sum XAS and their integration for GI geometry at 30 K, 13.5 K, 5.5 K and 1.2 K are shown in Figs. A4.3(a)-(c), A4.3(d)-(f), 4.4(a)-(c) and A4.4(d)-(f) for H = 0T and Figs. A4.5(a)-(c), A4.5(d)-(f), 4.6(a)-(c) and A4.6(d)-(f) for H=0.5T, respectively, in the same appendix. Using the P, Q and R values obtained for the NI and GI geometries (with and without dc magnetic field bias) at various temperatures (see Figs. A4.1-A4.6 in appendix (A)), we have calculated the m_{spin}.

The temperature variation of the magnetic spin moment parallel to the c-axis, calculated using the temperature-dependent XAS and XMCD signals measured in the NI geometry

with no dc bias field is shown in Fig. 4.7(a). For comparison, magnetization $M_{//c}(T)$ in units of μ_B per Fe^{3+} ion measured on a zero-field cooled crystal using MPMS-3 set-up with a field of 500 Oe applied along the c-axis is also shown in the same figure (Fig. 4.7(a)). It is evident from this figure that $M_{//c}(T)$ calculated using XMCD follows similar temperature dependence as that of $M_{//c}(T)$ measured by the magnetometer, even though the moments are lower for the XMCD results. We believe that this difference in moments is essentially due to the fact that the magnetization measurements were performed under 500 Oe field, while there was no such dc biasing field for XAS and XMCD measurements in the NI geometry. The difference between the two values increases with decreasing

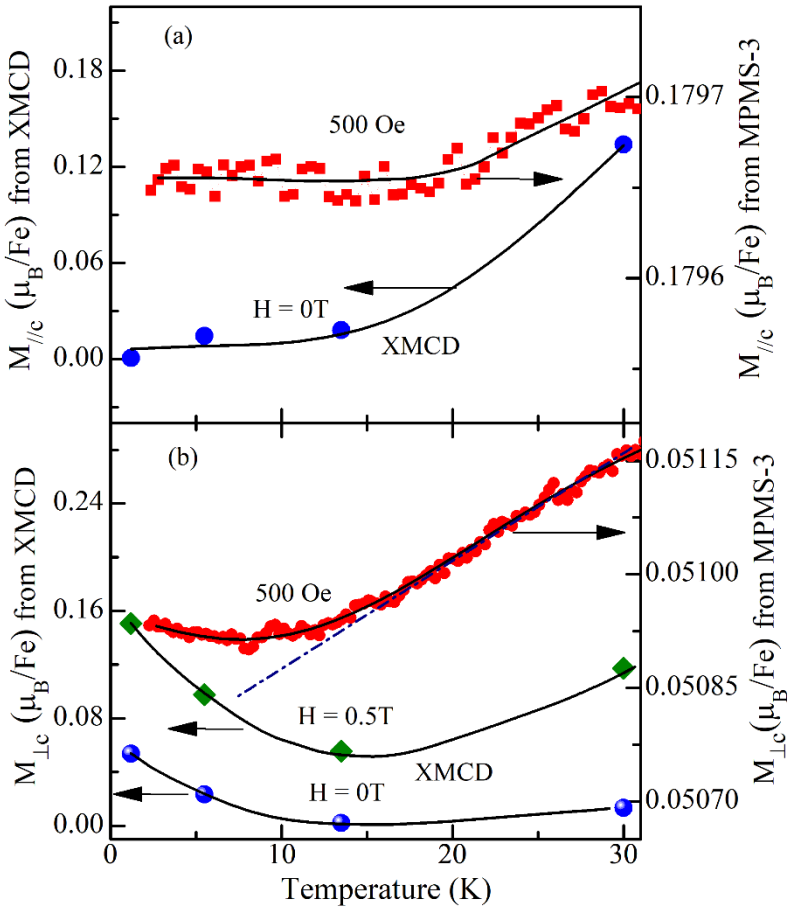

Figure 4.7: Comparison of the variation of the component of moments (a) longitudinal ($M_{//c}$) and (b) transverse components ($M_{\perp c}$) calculated using XAS, XMCD signal and dc magnetization measurements on the single-crystal.

temperature. This suggests that even a dc field of 500 Oe can ensure some alignment of the moments and hence large value of $M_{//c}(T)$ measured using the SQUID magnetometer when the thermal fluctuations are significantly reduced for $T \leq 13.5$ K. At high temperature, such as 30 K, the same field is not as efficient as at $T \leq 13.5$ K in aligning the moments in the field direction, and hence the difference between the XMCD and magnetometer results is much smaller at 30 K.

The temperature dependence of the transverse component of the spin moments calculated using temperature-dependent XAS and XMCD spectra for the GI geometry with H = 0 T and H = 0.5 T is shown in Fig. 4.7(b) along with the values obtained using the SQUID magnetometer under a dc field of 500 Oe applied perpendicular to the c-axis. It is evident that the magnetization $M_{\perp c}(T)$ plot, obtained using the XMCD signals for zero and 0.5 T dc field bias, shows an upturn for $T \lesssim 13.5$ K similar to that in the $M_{\perp c}(T)$ obtained by the magnetometer. Further, the increasing trend in the $13.5\ K \lesssim T \lesssim 30$ K range is also similar in both cases. This upturn in the $M_{\perp c}(T)$ suggests the possibility of some magnetic transitions at low temperatures which is the subject matter of next chapter. It is interesting to note that at T = 1.2 K, the $M_{\perp c}(T)$ measured using the magnetometer at 500 Oe and that calculated from the XMCD signals under dc field bias of 0.5 T are nearly equal suggesting that a 500 Oe field is sufficient to align some moments when the thermal fluctuations are nearly absent. The difference between the two values increases with increasing temperatures for H = 0 T field. Even with biasing field of 0.5 T, the XMCD measurements give lower value for $M_{\perp c}(T)$ as the field is applied with an off-set of 15^0 whereas in the magnetometer measurements, this field was applied perpendicular to the c-axis. But the point to note is that the difference between the two set of values of $M_{\perp c}(T)$ is lower for H = 0.5 T field than that without the field. Thus, both the dc magnetization M(T) and XMCD M(T) reveal: (1) a finite component of the magnetic moments in the ab-

plane also while the remaining component remains aligned parallel to the c-axis and (2) a non-monotonous behaviour of M (T) with an upturn around 13.5 K. We discuss the likely reason for this upturn in the next section.

4.3.4 XAS Studies at the Oxygen (O) K-edge

4.3.4.1 XAS Study at Oxygen K-edge at 1.2 K

The study of XAS spectra at the O K-edge is frequently used to probe the electronic energy states of the transition-metal ions in metal oxides and compounds [200,222,231,223–230] In the purely ionic model of oxygen (O^{2-}), one should not observe XAS spectra at the O K-edge due to $1s \rightarrow O2p^0$ excitation as can be inferred from its electronic configuration: $1s^2\ 2s^2\ 2p^6$. However, due to the hybridisation of the O-2p orbitals with the 3d orbitals of transition metal ions reduces the number of filled states of O-2p and enables the 1s→O-2p to Fe-3d excitation giving rise to peaks in the XAS spectra at the O K-edge [224].

To explore the local electronic structure of Fe 3d-orbitals in the ground state of BFO, we therefore analysed the XAS spectra of O at the K-edge recorded in the NI geometry at 1.2 K using RCP and LCP X-ray beams. To explore the electronic structure of Fe-3d orbitals, we have averaged the O K-edge XAS spectra recorded using LCP and RCP beams. XAS spectra thus obtained is equivalent to XAS spectra recorded using linearly polarised X-ray beam. Fig. 4.8 shows the averaged XAS spectra of BFO at 1.2 K. The XAS spectrum shown in this figure shows several well-defined peaks. If one ignores the influence of the core hole on the unoccupied bands [222], the peaks in the O K-edge spectrum may be related to the unoccupied density of states of oxygen. A comparison of the XAS spectrum of BFO at the O K-edge with those for Fe_2O_3, magnetite (Fe_3O_4) [232], $GaFeO_3$ [200], $(La,Sr)(Fe,Mn)O_3$ [223] reveals that the first region from 530 to 535 eV is mainly related to the electronic structure of 3d orbitals of Fe, i.e., peaks

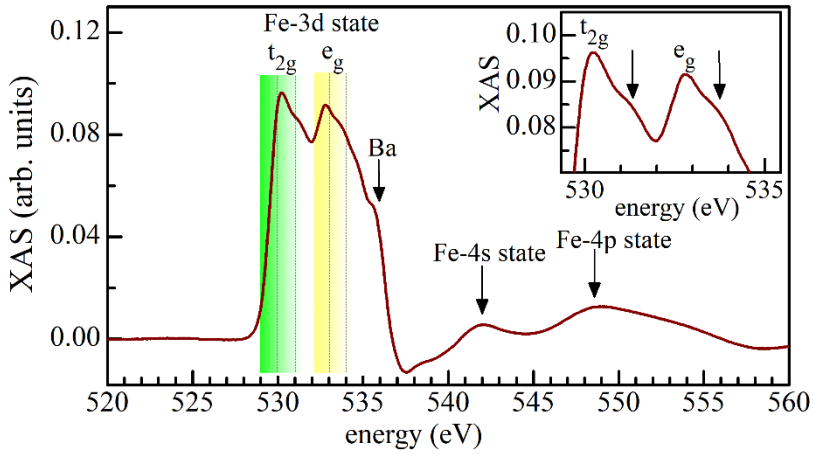

Figure 4.8: XAS spectra of oxygen at the K-edge recorded in normal incidence geometry at 1.2 K.

in the first region arise due to the transition from O-1s to O-2p Fe-3d hybridised orbitals. The second region from 540 to 560 eV in Fig. 4.8 consists of two broad peaks marked with arrows that are attributed to the O-2p Fe-4s4p hybridized states [202]. The small hump around ~ 537 eV is due to the mixing of the O-2p and Ba-5d states [233].

Since the first region (530 – 535 eV) at the O K-edge XAS spectrum contains information about the local electronic structure of Fe-3d orbitals, we focus our attention on the first region only. This region of the XAS spectrum shows two well-defined bands with a stronger peak in each band at ~ 530.23 eV and ~ 532.79 eV. The weaker intensity peak in the lower energy band occurs at ~ 531.12 eV while that in the higher energy band at ~ 533.47 eV. This is shown more clearly in the inset of Fig. 4.8. The splitting of the Fe-3d orbitals into two bands occurs due to the crystal field generated by the oxygen environment [202,224]. As mentioned earlier, Fe in BFO occupies three different oxygen environment as OH, TH and TBP. The local symmetry set by oxygen around the Fe decides the possible way of bonding among them i.e., hybridization between O-2p and Fe-3d orbitals. The Fe e_g-orbitals can approach directly towards O 2p-orbitals as in σ-bonding [224,234] for the OH environment and therefore show strong hybridization. On

the other hand, the Fe t_{2g}-orbitals are less hybridized with O 2p-orbitals due to the indirect approach as in the π- bonding for the OH environment [224,234]. This hybridization of the orbitals lifts the degeneracy of the five 3d energy levels in which the e_g levels are energetically higher than the t_{2g} energy levels for the OH environment, as noted in the context of FeO and α-Fe_2O_3 also [232]. A reverse scenario is observed for Fe in TH and TBP environments where the t_{2g} energy levels are now higher-lying than the e_g energy levels [222].

The XAS spectra at the O K-edge of BFO would contain contributions from Fe in OH, TH and TBP environments if there is hybridization of the Fe-3d orbitals with O-2p discussed above. Since the majority of Fe in the unit cell of BFO occupy OH positions, we have labelled the higher energy band as e_g and lower energy band as t_{2g} in the energy range ~ 530 eV to ~ 534 eV, respectively, of the O K-edge XAS spectrum shown in Fig. 4.8. As a result of the crystal field splitting, the five electrons of $3dFe^{3+}$ are distributed between e_g and t_{2g} bands with two electrons in the e_g and three in the t_{2g}. The crystal field splitting for the OH environment of Fe is schematically depicted in Fig. 4.9. The degeneracy of the energy levels in the two bands after the crystal field splitting may be

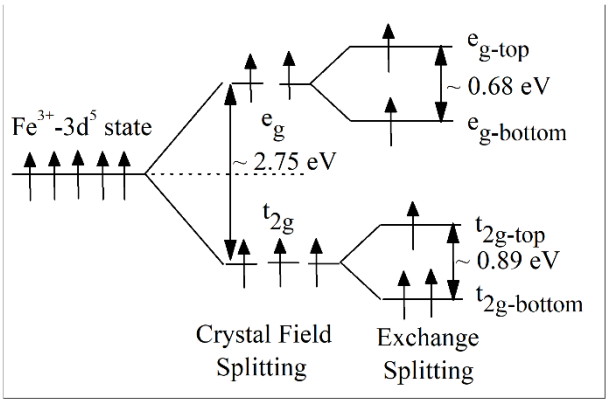

Figure 4.9: Schematic representation of splitting of $3dFe^{3+}$ orbitals in $BaFe_{12}O_{19}$ due to crystal field and exchange-correlation effects at 1.2 K.

lifted further due to exchange splitting [232]. One would, therefore, expect two energylevels in the e_g and three levels in the t_{2g} bands. But in the present case (Fig. 4.8), we observe two peaks each in the e_g and t_{2g} bands. This implies that one of the peaks in the t_{2g} band corresponds to the doubly degenerate t_{2g} level whereas the other peak in the t_{2g} and the peaks in e_g band correspond to singlet energy levels. This exchange splitting is also shown schematically in Fig. 4.9. The energy difference between the higher intensity and lower intensity peaks of the e_g band and the same peaks in the t_{2g} bands are found to be ~0.68 eV and ~ 0.89 eV, respectively. The intensity of the peaks in the t_{2g} and e_g bands is normally associated with the Fe 3d hole number [222,224,235]. Since the hybridization of Fe-3d e_g and O-2p is stronger than that of the Fe-3d t_{2g} and O-2p for the OH environment, one expects lower intensity of the e_g band [224]. However, the relative intensities may change significantly due to electronic exchange correlations and also due to non-stoichiometric effects [222]. To summarise, the study of O K-edge spectra of BFO at 1.2 K in the ~ 530 eV to ~ 534 eV region provides evidence for the crystal field splitting of the Fe-3d orbitals and also the splitting of the e_g and t_{2g} bands due to exchange-correlation effects. The estimated crystal field from the difference in the energy of the middle of e_g and middle of t_{2g} bands is found to be 2.75 eV which is quite large. Similar large crystal field splitting has, however, been observed in TiO_2 (~ 2.4 eV) and also in 4d and 5d transition metal oxides (~3.5 eV) [224].

4.3.4.2 XAS Spectra at the Oxygen K-edge as a Function of Temperature

As pointed out in the previous section, the degeneracy of the Fe-$3d^5$ state gets lifted due to the crystal field which splits the Fe-3d level into t_{2g} and e_g bands, which further split due to the exchange correlation effects. As discussed in the previous section, the XMCD profile at 1.2 K and 5.5 K is inverted at T = 13.5 K (see Fig. 4.4). Further, there is an upturn in the $M_{\perp c}$ (T) obtained by XMCD around the same temperatures (see

Fig. 4.7). To verify whether both these are related to the hybridised states of Fe-3d orbitals, we depict the temperature dependence of XAS spectra at the O K-edge in Fig. 4.10. Qualitatively, it is evident from this figure that the intensity of the e_g band with respect to the t_{2g} band decreases with decreasing temperature. Since intensity of the t_{2g} and e_g bands in the O K-edge spectra is directly related with the strength of the O 2pFe-t_{2g} and O 2pFe-t_{2g} hybridizations, the reduction in relative intensity of the e_g band with temperature signifies the decrease in the O-2p weight into e_g band of Fe-3d orbitals.

To quantify the temperature-dependent effects on the Fe-3d electronic states, the lower $t_{2g\text{-bottom}}$ and higher $t_{2g\text{-top}}$ energy peaks of the t_{2g} band and the $e_{g\text{-bottom}}$ and $e_{g\text{-top}}$ of the e_g band are listed in Table 4.4. The bandwidth of the e_g and t_{2g} bands after crystal field splitting are listed in Table 4.5. Table 4.6 lists the change in crystal field splitting and exchange splitting of both the t_{2g} and e_g bands. It is evident from these tables that the

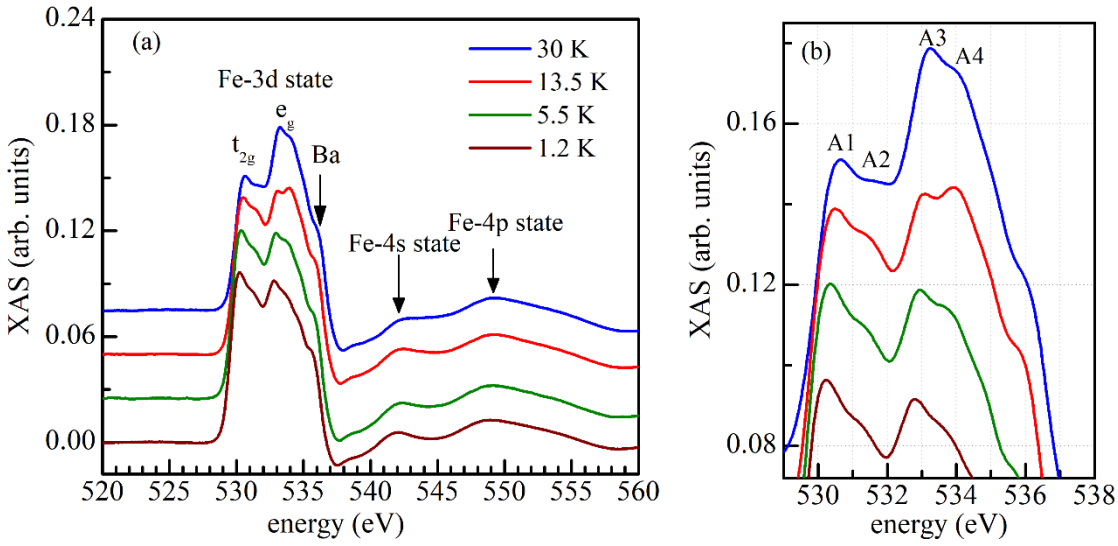

Figure 4.10: (a) XAS spectra at the O K-edge recorded in the NI geometry at various temperatures. (b) XAS spectra on a zoomed scale. Peaks A1, A2, A3 and A4 in (b) are labelled as $t_{2g\text{-bottom}}$, $t_{2g\text{-top}}$, $e_{g\text{-bottom}}$ and $e_{g\text{-top}}$, respectively. All the curves in (a) are shifted along the y-axis by 0.025.

exchange splitting for the e_g band changes by 0.17 eV between 13.5 and 5.5K, suggesting its role in the inversion of XMCD profile shapes in Fig. 4.4 and upturn in $M_{\perp c}$ in Fig. 4.7 around 13.5 K. However, more theoretical insight is required to understand the exact role of crystal field splitting and exchange-correlation energies on the XMCD profile shapes as well as the upturn in the $M_{\perp c}$ around 13.5K. As discussed in the next chapter, two additional spin-glass transitions emerge for $T \lesssim 20$ K in BFO and we believe that the change in the exchange splitting around this temperature might be affecting the exchange anisotropy, which in turn can lead to freezing of the longitudinal and transverse components of spins, discussed in the next chapter, as per the theory of Bray et al., [236].

Table 4.4: Energy of the peaks t_{2g} and e_g bands observed at the O K-edge spectra recorded in NI geometry at various temperatures.

T (K)	$t_{2g\text{-bottom}}$ peak	$t_{2g\text{-top}}$ peak	$e_{g\text{-bottom}}$ peak	$e_{g\text{-top}}$ peak
30 K	530.63 eV	531.67 eV	533.23 eV	534.05 eV
13.5 K	530.49 eV	531.37 eV	533.038 eV	533.94 eV
5.5 K	530.35 eV	531.24 eV	532.94 eV	533.67 eV
1.2 K	530.23 eV	531.12 eV	532.79 eV	533.47 eV

Table 4.5: Energy of the t_{2g} and e_g bands observed at the O K-edge spectrum recorded in NI geometry at various temperatures.

T (K)	Middle of t_{2g} = $(t_{2g\text{-bottom}} + t_{2g\text{-top}})/2$	Middle of e_g = $(e_{g\text{-bottom}} + e_{g\text{-top}})/2$	Crystal field splitting	Band width of t_{2g} = $(t_{2g\text{-top}} - te_{2g\text{-bottom}})$	Band width of e_g = $(e_{g\text{-top}} - e_{g\text{-bottom}})$
30 K	531.15 eV	533.64 eV	2.49 eV	1.04 eV	0.82 eV
13.5 K	530.93 eV	533.489 eV	2.559 eV	0.88 eV	0.90 eV
5.5 K	530.795 eV	533.305 eV	2.509 eV	0.89 eV	0.73 eV
1.2 K	530.375 eV	533.13 eV	2.75 eV	0.89 eV	0.68 eV

Table 4.6: Change in crystal field and exchange splitting energies with increase in temperature.

Temperatures	Change in crystal field splitting energy	Change in exchange splitting energy of t_{2g} band	Change in exchange splitting energy of e_g band
30 K to 13.5 K	0.069 eV	0.16 eV	0.08 eV
13.5 K to 5.5 K	0.05 eV	0.01 eV	0.17 eV
5.5 K to 1.2 K	0.24 eV	0 eV	0.049 eV

4.4 Conclusions

(1). We located the Curie temperature of the ferrimagnet phase of BFO as T_c ~ 714 K using high-temperature dc magnetization studies.

(2). $M_{\perp c}(T)$ as well as magnetic anisotropy ($\frac{M_{\perp c}}{M_{//c}}$) shows a maximum at ~ 45 K suggesting a magnetic phase involving the basal plane component of the spins.

(3). The canted nature of $3dFe^{3+}$ spins in BFO with respect to the c-axis was confirmed by temperature and incident angle dependent XAS and XMCD studies.

(4). Using XAS studies at the O K-edge, we presented evidence for the splitting of the Fe-3d orbitals into e_g and t_{2g} bands due to crystal field effects.

(5). These bands split further into two energy levels each due to exchange-correlation effects.

(6). There is a significant change in the exchange splitting between 13.5 K and 5.5 K which may be responsible for the change in the XMCD profile shapes and the upturn in $M_{\perp c}(T)$ obtained by XMCD studies. However, Theoretical calculations are required to confirm this hypothesis.

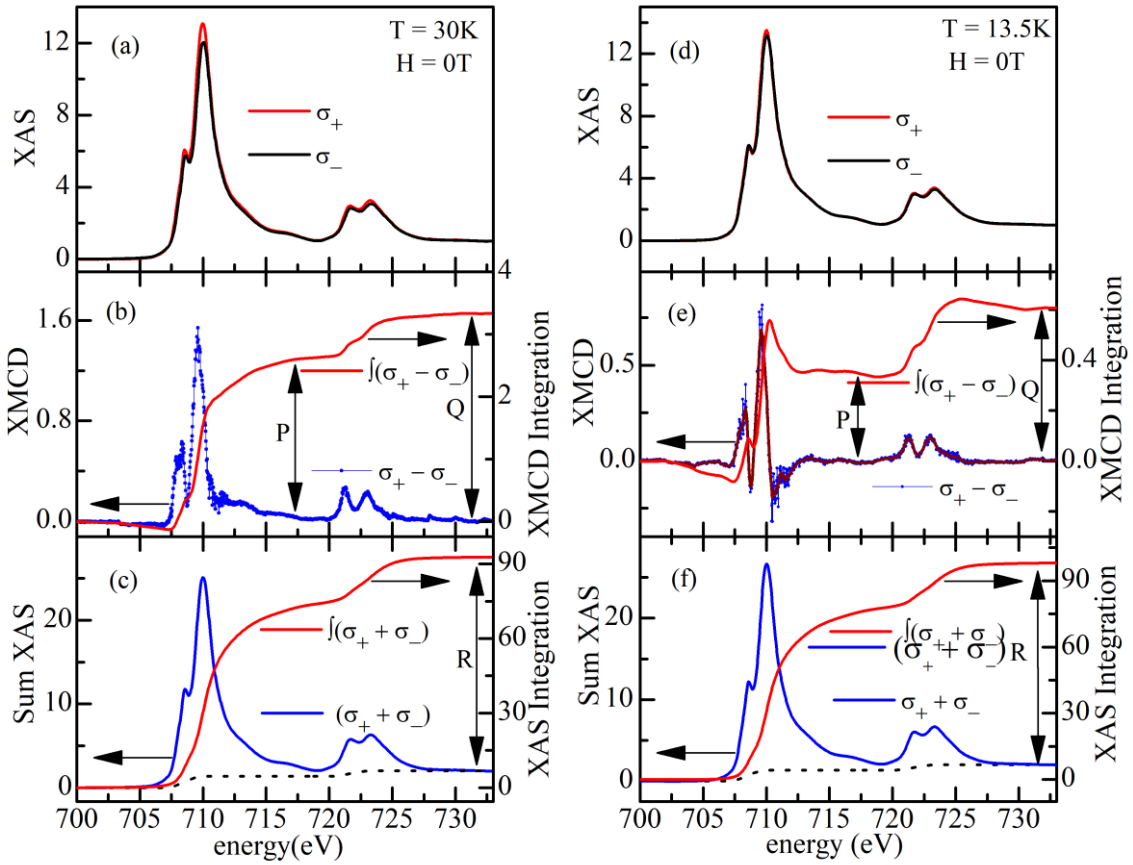

Figure A4.1: (a) and (d) Normalised XAS spectra at the Fe $L_{2,3}$-edges. (b), (e) and (c), (f) shows the XMCD signal and summed XAS with their integration measured in normal incidence geometry with field of 0 T at 30 K and 13.5 K, respectively. The dotted line in (c) and (f) is the two-step-like function used for edge jump removal before XAS integration.

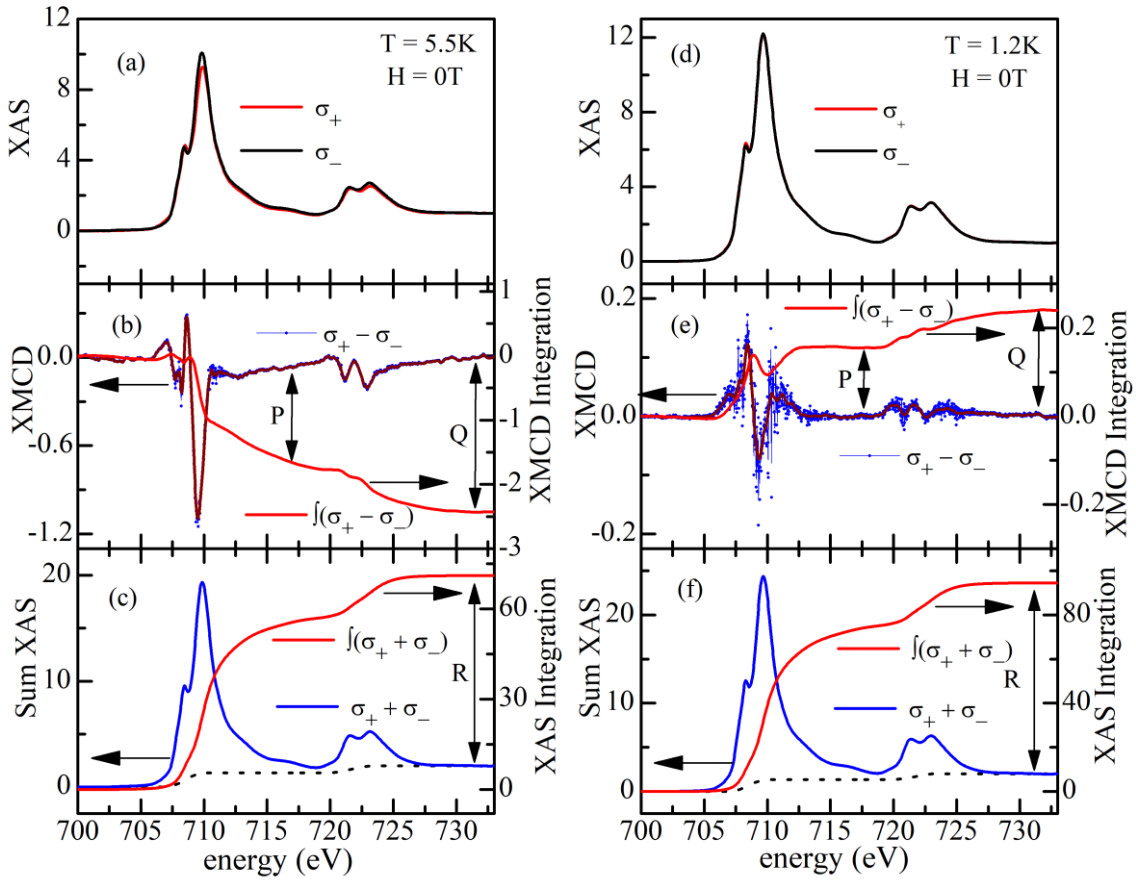

Figure A4.2: (a) and (d) Normalised XAS spectra at the Fe $L_{2,3}$-edges. (b), (e) and (c), (f) shows the XMCD signal and summed XAS with their integration measured in normal incidence geometry with field of 0 T at 5.5 K and 1.2 K, respectively. The dotted line in (c) and (f) is the two-step-like function used for edge jump removal before XAS integration.

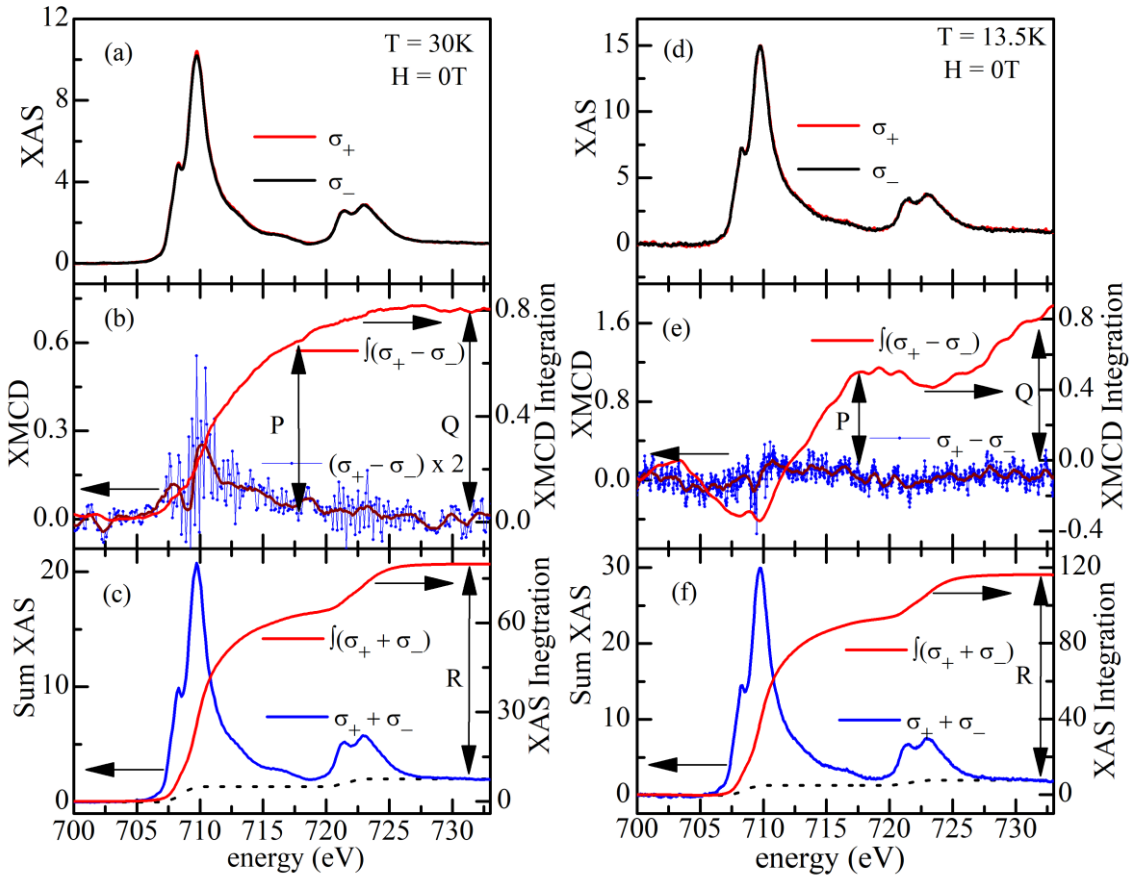

Figure A4.3: (a) and (d) Normalised XAS spectra at the Fe $L_{2,3}$-edges. (b), (e) and (c), (f) shows the XMCD signal and summed XAS with their integration measured in grazing incidence geometry with field of 0.5 T at 30 K and 13.5 K, respectively. The dotted line in (c) and (f) is the two-step-like function used for edge jump removal before XAS integration.

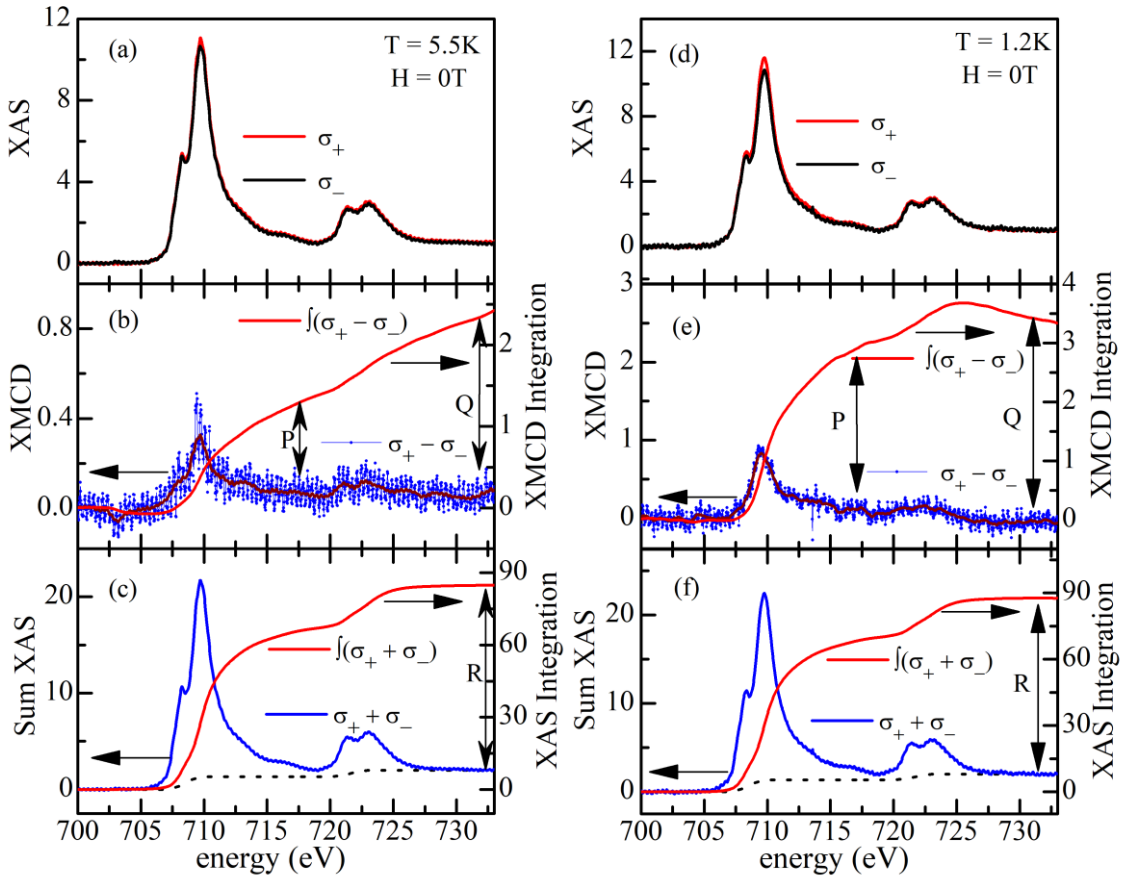

Figure A4.4: (a) and (d) Normalised XAS spectra at the Fe $L_{2,3}$-edges. (b), (e) and (c), (f) shows the XMCD signal and summed XAS with their integration measured in grazing incidence geometry with field of 0 T at 5.5 K and 1.2 K, respectively. The dotted line in (c) and (f) is the two-step-like function used for edge jump removal before XAS integration.

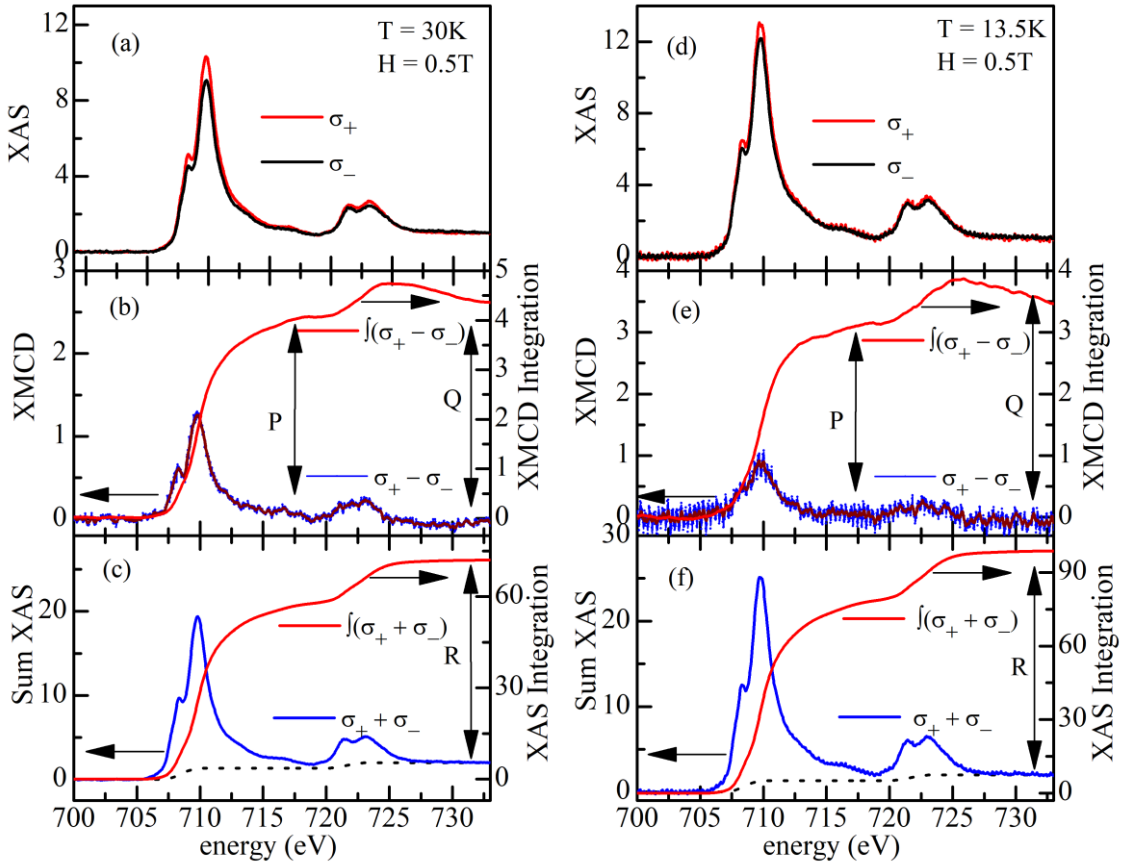

Figure A4.5: (a) and (d) Normalised XAS spectra at the Fe $L_{2,3}$-edges. (b), (e) and (c), (f) shows the XMCD signal and summed XAS with their integration measured in grazing incidence geometry with field of 0.5 T at 30 K and 13.5 K, respectively. The dotted line in (c) and (f) is the two-step-like function used for edge jump removal before XAS integration.

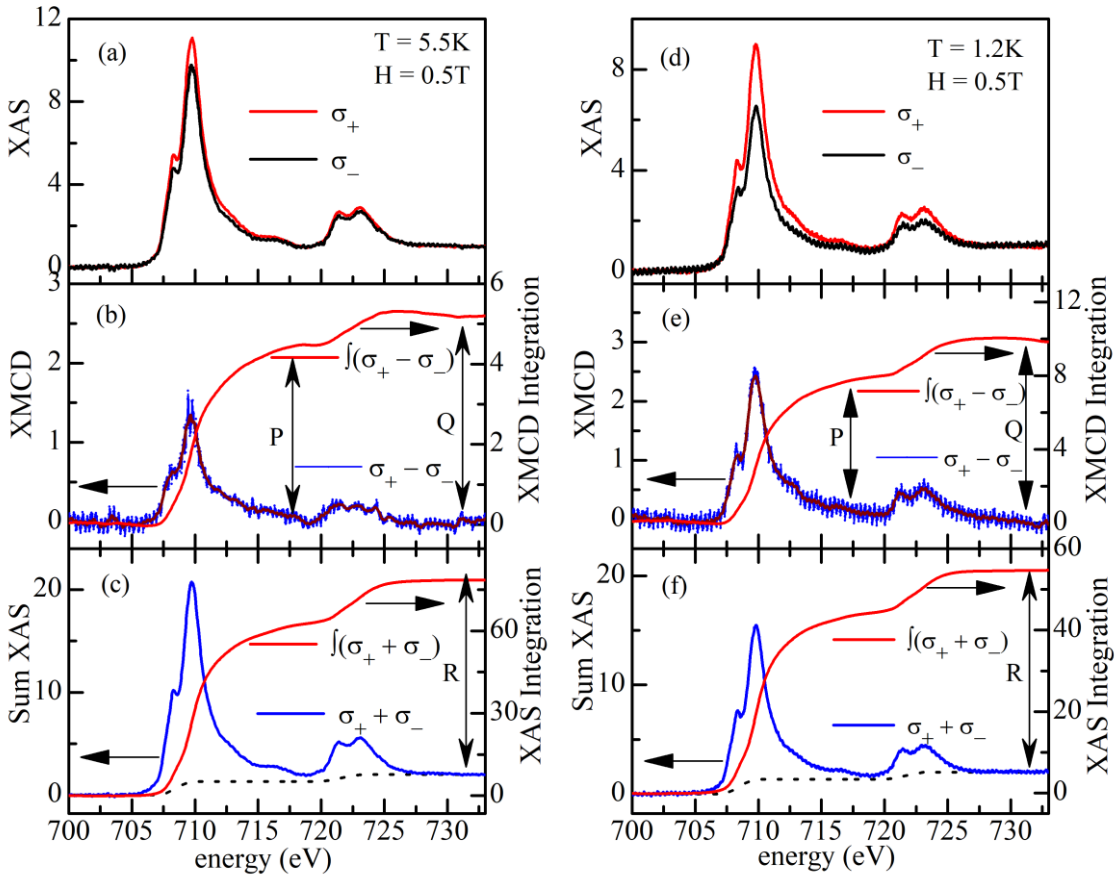

Figure A4.6: (a) and (d) Normalised XAS spectra at the Fe $L_{2,3}$-edges. (b), (e) and (c), (f) shows the XMCD signal and summed XAS with their integration measured in grazing incidence geometry with field of 0.5 T at 5.5 K and 1.2 K, respectively. The dotted line in (c) and (f) is the two-step-like function used for edge jump removal before XAS integration.